Research Article | Vol. 32, No. 19 / 9 Sep 2024 / Optics Express 33875
Optics EXPRESS

Scaling narrowband THz generation to large apertures in $LiNbO_3$ and KTP

N. H. Matlis,[1] H. T. Olgun,[1] C. Rentschler,[1] K. Ravi,[1] T. Taira,[2,3] H. Ishizuki,[2,3] and F. X. Kärtner[1,4,5,*]

[1]Center for Free-Electron Laser Science CFEL, Deutsches Elektronen-Synchrotron DESY, Notkestr. 85, 22607 Hamburg, Germany
[2]Division of Research Innovation and Collaboration, Institute for Molecular Science, 38 Myodaiji, Okazaki, Aichi 444-8585, Japan
[3]Innovative Light Sources Division, RIKEN SPring-8 Center, 1-1-1 Kouto, Sayo-cha, Sayo-gun, Hyogo 679-5148, Japan
[4]The Hamburg Centre for Ultrafast Imaging, University of Hamburg, Luruper Chaussee 149, 22761 Hamburg, Germany
[5]Department of Physics, University of Hamburg, Luruper Chaussee 149, 22761 Hamburg, Germany
*franz.kaertner@desy.de

Abstract: Millijoule-scale pulses of multicycle terahertz radiation (MC-THz) are increasingly being pursued as drivers for applications requiring high-fields and high spectral brightness. An attractive approach for generating high peak-power MC-THz pulses is nonlinear optical down-conversion of laser pulses in periodically-poled crystals. A principal limitation to the yield, however, is the small (sub-centimeter) apertures of commercially-available crystals which restrict the amount of laser energy that can be used. Here, we explore MC-THz generation by down conversion in two types of large-aperture media for which periodic poling has been achieved in different ways: (1) extension of traditional, voltage-based poling of bulk material to larger (centimeter) scales; and (2) manual poling by assembly of large aperture sub-millimeter thick wafers in alternating orientations. We explore the dependence of efficiency on laser peak fluence and crystal length for both types of media and extend upon previous work with the wafer approach by increasing the number of wafers in the stack, implementing cryogenic cooling and testing an alternate material: potassium titanyl phosphate (KTP). Driving with up to 0.2 J, half-picosecond laser pulses centered at 1,030 nm, we obtain conversion efficiencies of up to 0.14%, resulting in ~1% bandwidth MC-THz pulses of up to 207 μJ.

1. Introduction

High-energy, high-field pulses of narrowband THz radiation have a wide range of applications including coherent control of matter [1], enhancing ultrafast electron-diffraction instruments [2] and powering the next generation of compact accelerators and table-top x-rays sources [3,4,5]. For some applications [5], sub-percent bandwidth pulses with energies of tens of millijoules are required which is far beyond what has been demonstrated to date. Nonlinear down-conversion of laser pulses is one of the most promising approaches for the realization of such MC-THz sources. However, the efficiency for optical-to-THz conversion is typically very low, requiring use of high-energy lasers as drivers in order to reach moderate THz pulse energies. The low conversion efficiency (CE) is largely attributable to the orders-of-magnitude difference in photon energies between the optical and THz domains. Due to this discrepancy, even a 100% conversion of photons translates into an energy efficiency of order 0.1% for sub-THz frequencies. The CE of a nonlinear process can generally be increased by ramping up the fluence of the drive-laser

#533354 https://doi.org/10.1364/OE.533354
Journal © 2024 Received 27 Jun 2024; revised 15 Aug 2024; accepted 16 Aug 2024; published 4 Sep 2024

Optics EXPRESS

pulse, but the dependence of CE on fluence eventually rolls over and saturates. Increasing the fluence beyond this point then risks irreversible damage of the conversion medium. Further increases in CE can be obtained by fine-tuning the spectral, temporal and spatial properties of the drive pulses to optimize phase matching in the crystal [6,7,8,9]. As a result of this optimization (both of the fluence and other laser-pulse properties), "cascading" of the nonlinear interaction (in which each optical photon participates multiple times in the conversion process [10,11]) occurs, multiplying the CE beyond the ratio of the photon energies. However, despite simulations predicting optimized efficiencies in the range of multiple percent [7,11,12], in practice, the highest conversion efficiency achieved for MC-THz generation in the sub-THz regime is still about one percent [6].

To significantly increase the yield of THz therefore requires either pushing the maximum achievable fluence to higher levels (e.g., by exploring alternate materials [9]) or scaling of the nonlinear process to larger apertures to accommodate larger pulse energies. For sub-THz frequencies, lithium niobate ($LiNbO_3$) is currently the material of choice and has been used to demonstrate multiple records in THz generation [6,13–17]. This preference is traceable to its high effective nonlinear optical coefficient (d_{33} = 168 pm/V) [18] and its mature level of development stemming from its ubiquitous application across optics-related industries. In $LiNbO_3$, the saturation fluence is typically in the range of 100–500 mJ/cm^2, depending on the pumping configuration. Considering that suitable lasers for THz generation exist with multi-Joule pulse energies, crystal apertures in the centimeter scale are therefore needed. Although bulk $LiNbO_3$ crystals (suitable, e.g., for single-cycle THz generation [19–21]) can easily be fabricated with apertures of 30–40 mm, periodically-poled $LiNbO_3$, which is the format most often used for narrowband THz generation (via quasi-phase matching, QPM), can currently only be obtained commercially with apertures of 5 mm or less. This limitation is connected to the increasing difficulty of imprinting a periodic poling structure in bulk $LiNbO_3$ as the crystal aperture increases (in the poling direction).

Two approaches currently being pursued to overcome this limitation are: (1) extension of the standard (voltage-based) poling process to larger apertures [22–25], and (2) manual assembly of periodically-poled macro-crystals by stacking wafers of a bulk material with alternating orientations [16,26]. The standard approach involves applying sequences of high-voltage pulses to spatially-patterned electrodes on either side of a bulk material to induce local reversal of the ferroelectric polarity. This approach is highly material specific and is strongly affected by small changes to the composition such as addition of dopants like magnesium oxide (MgO). Despite the complications it adds to the poling process, doping with MgO is highly prevalent due to its ability to mitigate the photo-refractive effect (PRE) which can cause material damage and hence limits the applied fluence in $LiNbO_3$ [27]. Over the past decade, researchers at the Institute for Molecular Science in Japan have made significant progress in fabricating large-aperture, periodically-poled, MgO-doped $LiNbO_3$ (LA-MgO:PPLN) devices, leading to poled dimensions up to 12 mm [22–25] and opening up a highly promising avenue for scaling to larger energies. While a large body of work exists demonstrating THz generation in smaller aperture devices in various pumping configurations, only one work has so far demonstrated THz generation in 10 + mm aperture PPLN devices [15], and no work has so far been done with a compressed, short-pulse pumping configuration which remains the most common and, thus, the most relevant for bench-marking purposes. In particular, while it has been shown that driving with lasers having a pulse train or otherwise periodically-modulated temporal structure improves the conversion efficiency [6,8,14,15,28], single-pulse drivers are much less sensitive to phase-matching conditions, allowing a more reliable comparison between different conversion media.

The second (wafer-based) approach, first demonstrated by Thompson et al. in 1976 in the context of second harmonic generation [29], offers a number of advantages over the voltage-based

Optics EXPRESS

concept. First, significant increases in aperture size are possible, as wafers of relevant thickness can be produced in the range of multiple centimeters. Second, fine-tuning and hence optimization of the crystal length can be done straight-forwardly. And third, unlike the voltage-based approach, for which development of the poling technique in new materials can take years to perfect, the wafer approach is inherently well adapted to exploring a wide variety of materials. These advantages come at the cost of multiple technical complexities. First, the large number of interfaces make wafer stacks prone to large transmission losses for both the optical driver and the generated THz. The optical losses can be mitigated by anti-reflection coating of all surfaces, but are increasingly difficult to implement for the thinner wafers needed for higher THz frequencies. Meanwhile, to avoid THz losses requires that the gaps between wafers are significantly smaller than the wavelength, i.e., in the range of a few microns. Cryogenic cooling, which improves efficiency by reducing the THz absorption coefficient by an order of magnitude [13,30] is also complicated by the large aspect-ratio of the wafers. Finally, to reach sufficient crystal lengths to optimize the interaction requires a large number of periods [8], and hence a large number of wafers. The optimum length depends on the details of the drive laser. For single-pulse drivers, where efficiencies of order 0.1% – 0.2% can be expected, interaction lengths in the range of several millimeters are sufficient [13]. However, for the temporally- and spectrally-structured drive-laser pulses capable of reaching efficiencies near 1%, interaction lengths in the range of multiple centimeters are needed [6,11,12,31]. To achieve these crystal lengths requires tens to hundreds of wafers, depending on the excitation frequency, for which it becomes challenging to ensure the uniformity and quality of the poling (i.e., the wafer spacing and the associated inter-wafer gaps). The last few years have seen major steps forward in testing the feasibility of the wafer approach, with demonstrations of the ability to control optical losses and scale to large energies for short, room-temperature wafer stacks (12 wafers = 3.6 mm) with lower generated frequencies (160 GHz) [16] as well as demonstrations of crystal-length fine tuning and extension to slightly larger wafer numbers (20 wafers = 3.1 mm) and higher frequencies (390 GHz) [26]. Much work remains, however, to mature this technology to a similar level as the voltage-based one.

Here we explore high-energy THz generation in a compressed, short-pulse pumping configuration using both voltage-poled LA-MgO:PPLN devices [25] as well as in-house assembled, manually-poled wafer-stack devices of two different materials. In the first type of experiments, devices with 5% MgO-doped LA-MgO:PPLN with 330 μm poling period, apertures of 10×15 mm, and lengths varying from 12–36 mm were used. We record maximum conversion efficiencies over 0.14%, matching results achieved with smaller, commercially available PPLN devices [13], but thanks to the large aperture, we achieve pulse energies of over 100 μJ, which is over an order of magnitude higher than previous results in this configuration. In the wafer experiments, we extend upon previous work in several key regards. First, the maximum number of wafers in a stack is increased to over 40, resulting in a maximum crystal length of 9.5 mm which is 3x larger than previously demonstrated. To address the issue of THz absorption, which becomes increasingly severe for larger stacks, we implement cryogenic cooling for the first time. At lower temperatures and longer crystals, however, the damage threshold also typically reduces due to PRE and various nonlinear phenomena, limiting the applicable fluence. Exploration of alternate materials with potential for high conversion efficiency and higher damage threshold is thus strongly motivated. We therefore also test wafer stacks of potassium titanyl phosphate (KTP), which is known to have a high damage threshold [32,33], highlighting the flexibility of the wafer-based approach and complementing recent promising experiments using small-aperture, voltage-poled KTP crystals [9]. We achieve THz pulse energies up to 207 μJ in $LiNbO_3$ with conversion efficiencies of up to 0.1% and pulse energies up to 125 μJ in KTP with conversion efficiencies of over 0.13%. Our results help to confirm the viability of both large-aperture approaches and highlight the advantages and disadvantages of each.

Optics EXPRESS

2. Experimental setup

Optical pulses for driving the narrowband THz generation were sourced from a commercial laser system of wavelength 1.03 μm and producing pulses with energy up to 200 mJ and pulse durations down to 400 fs at a repetition rate of 52 Hz. The beam size at the interaction position was 6.3 mm x 5.7 mm ($1/e^2$ radius). Although the use of spectrally- and temporally-tailored laser pulses has been shown to yield higher conversion efficiencies [7,11,12,14,15,34], short, fully-compressed pulses are more versatile for testing new conversion media in that the experimental setup is insensitive to changes in poling period or crystal material. As a result, variations in performance can be more easily be attributed to the properties of the crystals rather than to the properties of the optical driver. In addition, the larger body of work using compressed pulses make them more suitable for bench-marking purposes.

Two types of periodically-poled media were tested: voltage-poled, MgO-doped $LiNbO_3$ and manually-poled wafer stacks of both MgO-doped $LiNbO_3$ and KTP. The voltage-poled devices, which were 5% MgO doped, were provided in pieces of aperture 10×15 mm and length 40 mm with a 330 μm period poling structure imprinted over the central 36 mm section. These blanks were then commercially cut and polished into pieces of length 12, 16, 20, 24 and 36 mm to allow characterization of the length dependence of the THz-generation process. The surfaces of all devices were uncoated except for the 36 mm piece which (in a previous experiment) was anti-reflection (AR) coated for an 800 nm optical driver. The wafers were commercially sourced from multiple vendors in multiple shapes and dimensions. The $LiNbO_3$ wafers were obtained both with round cross-sections of 25.4 mm diameter and 300 μm thickness (600 μm period) as well as in 25×26 mm rectangular cross-sections of thickness 200 μm. The KTP wafers were obtained with 10×10 mm apertures and 250 μm thickness. All wafers were AR coated for the 1.03 μm drive laser.

The experimental setup is illustrated schematically in Fig. 1. All devices except for the round $LiNbO_3$ wafer stacks were installed in a liquid-nitrogen cryostat to allow cryogenic cooling to ~89 K. Custom copper mounting structures were developed to ensure good thermal contact of the devices to the cold surface for efficient cooling, and (in the case of the wafer stacks) to press the wafers together for achieving a uniform poling. The laser beam passed through the periodically-poled devices generating THz in a collinear geometry. In the case of the voltage-poled PPLNs and the KTP wafer stacks, a ceramic mask with a 10×10 mm aperture was used to vignette the beam and avoid stray light hitting sensitive components. As a result of this vignetting, the maximum energy incident on the device was less than the total available in the beam. To separate the laser from the THz after the interaction and minimize laser contributions to noise or damage to the detection system, a 1 cm thick polytetrafluoroethylene (PTFE) and two 2 mm sheets of black polyethylene (PE) were inserted into the beam. Two polymethylpentene (TPX) lenses with focal lengths of 75 mm and 50 mm were used to collect and concentrate, respectively, the THz radiation onto a pyroelectric THz detector (Gentec THZ9B) for energy measurements, or alternatively, to a Michelson interferometer for measurements of the THz spectrum.

Each experimental configuration was characterized by measuring THz yield versus the laser-pulse energy, which was controlled using a half-wave plate (HWP) and thin-film polarizer (TFP) after the last laser amplification stage and before the pulse compressor. For statistics, up to 30 measurements of the yield were taken at each laser pulse energy. The THz yield and the conversion efficiency were calculated by considering the laser and THz pulse energies within the conversion medium in order to evaluate the performance of the conversion process abstracted from practical issues such as interface and transport losses. The internal THz energy was calculated by considering Fresnel losses at the crystal exit and transmission losses through the cryostat exit window, the PTFE and PE plates and both TPX-lenses (Table 1). The Fresnel losses were calculated based on known values of the index of refraction and assuming normal incidence

Optics EXPRESS

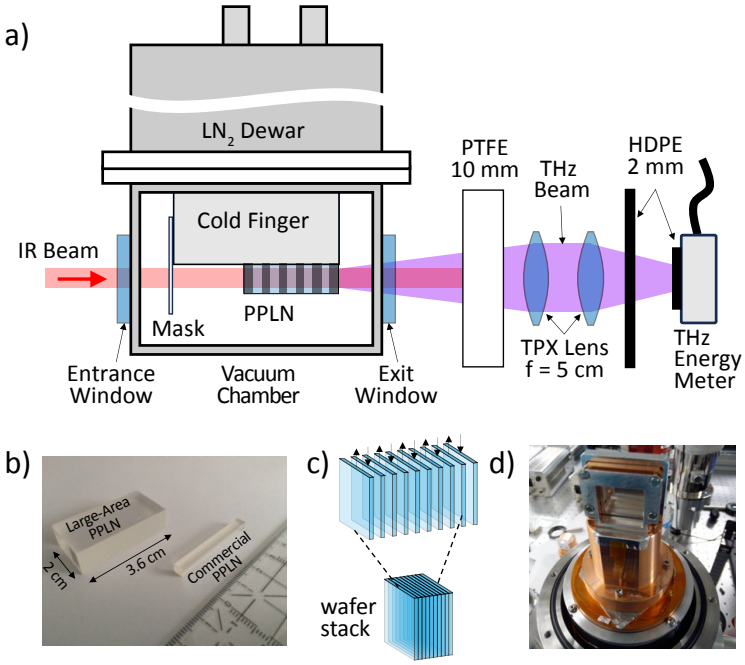

Fig. 1. Experiment setup. (a) Optical layout showing the periodically-poled device mounted to the cold finger inside the cryostat. A mask installed before the device is used to prevent damage caused by illumination of the edges. One Teflon and two HDPE plates are used to block the transmitted pump beam, and two TPX lenses collect and refocus the THz energy onto the detector. (b) Photo of large-area custom PPLN side by side with a 4×4 mm aperture commercial PPLN. (c) Schematic showing assembly of a periodically-poled macro crystal from a stack of alternatingly-oriented wafers. (d) Photo of a wafer stack mounted via a custom holder to the cold-finger of the cryostat.

while the transmission losses through various elements were individually measured using a commercial THz time-domain spectrometer (THz-TDS). For the laser, the geometrical losses due to the beam clipping at the crystal aperture were measured in addition to the Fresnel losses and the net transmission of the laser through the stack was measured to evaluate the performance of the coatings.

Table 1. THz losses in beamline elements

Frequency (GHz)	Teflon (%)	TPX (%)	Polyethylene (%)	Vacuum window (%)
160[a]	7	23	31	-
250	9	20	32	33
270	2	15	27	33
302	2	9	37	34
324	6	9	32	35

[a]The 160 GHz scans were performed only at room temperature, therefore the vacuum window was not needed.

Optics EXPRESS

3. Results

3.1. Results using voltage-poled LA-MgO:PPLN devices Λ_{PPLN} = 330 μm

Figure 2 shows a summary of the THz yield obtained using the voltage-poled crystals of 5% MgO:PPLN with a poling period of . For each of the five crystal lengths, the THz yield was measured as a function of laser-pulse energy at room temperature (RT) (Fig. 2(a)) and cryogenic temperature (CT) (Fig. 2(d)). The maximum yield depended strongly on crystal length and temperature, varying from 5 μJ to 50 μJ at RT and from 50 μJ to over 100 μJ at CT, with the best performance being obtained for the shortest crystal (12 mm) at both temperatures. As expected, cryogenic cooling significantly improves the THz yield by reducing THz absorption, and the improvement becomes increasingly important with crystal length. For example, with the 12 mm crystal, the improvement is roughly a factor of two, while for the 36 mm crystal the improvement is a factor of ten. The corresponding conversion efficiencies versus peak laser fluence are shown in Fig. 2(b) and Fig. 2(e), respectively. The peak efficiency also depends strongly on crystal length and varied from 0.015% to 0.06% at RT, and from 0.09% to 0.14% at CT, with the shortest crystal yielding the highest efficiency.

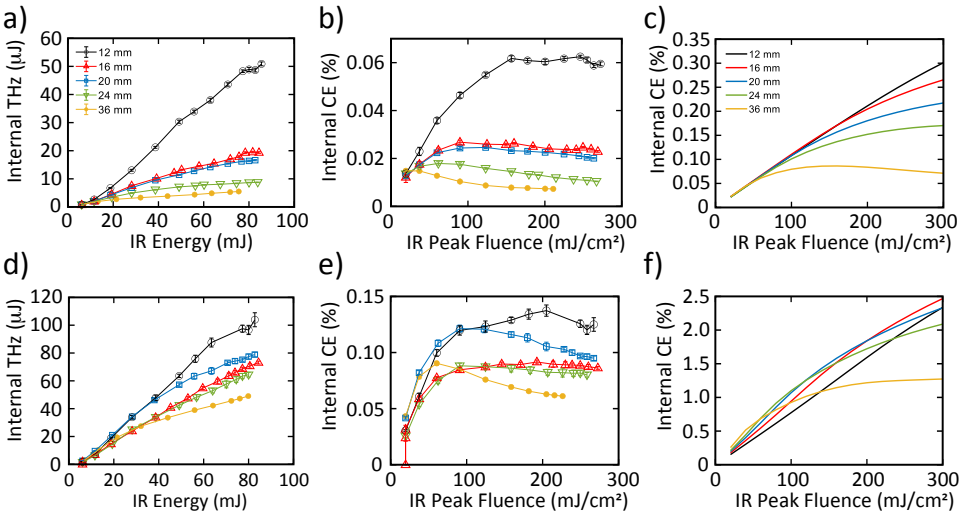

Fig. 2. Results for LA-MgO:PPLNs of length: 12, 16, 20, 24 and 36 mm. (a),(d) THz yield vs laser energy for RT and CT, respectively. (b),(e) internal efficiency vs laser fluence for (a) and (d), respectively. (c),(f) Simulation results corresponding to the data in (b) and (e), respectively.

The saturation of the CE is very evident in Figs. 2(b),(e) and occurs at a relatively low fluence in the range of 20–200 mJ/cm^2, depending on crystal length and temperature. The trend with crystal length is also very clear, with longer crystals exhibiting a lower saturation fluence. The dependence of the peak CE and the saturation fluence on crystal length can be understood straight-forwardly by considering the physics of quasi-phase matching [7,17] combined with modification of the pump pulse due to nonlinear effects. Due to the difference between the THz phase- and optical group velocities, the optical pulse out-runs the THz wave, creating a new THz cycle for each period of the PPLN traversed. The amplitude of each cycle, once it exits the crystal, is then determined by the intensity of the laser pulse and the attenuation experienced traversing the crystal from the point of creation. Cycles created at the beginning of the crystal therefore experience the greatest attenuation. The expected waveform of the THz pulse therefore consists of as many cycles as there are poling periods, with an amplitude that exponentially decays behind

Optics EXPRESS

the driver pulse. The scale of this decay is given by the "absorption length", $L_{abs} \equiv 1/\alpha$, where α is the absorption coefficient. Based on this picture and ignoring depletion of the pump, the THz yield should increase with crystal length as additional cycles are created, but should saturate (i.e., reach a steady state) once the absorption length is exceeded and the first cycle is fully attenuated. The physics in the undepleted regime is easily captured analytically. Following the approach outlined in [8,12,17], the conversion efficiency in this regime can be written as

$$\eta(L) \approx \frac{4d_{eff}^2\Omega_{PM}^2 F_0}{\pi^2\varepsilon_0 c^2 n^2(\omega) n(\Omega_{PM}) \Delta n}\left[\frac{1-e^{-\alpha(\Omega_{PM})L}}{\alpha(\Omega_{PM})}\right] e^{-\frac{1}{2}(\Omega_{PM}\Delta T)^2} \tag{1}$$

where d_{eff} is the effective quasi-phase-matched nonlinear coefficient, F_0 is the peak optical fluence, ΔT is the 1/e duration of the optical pulse, ε_0 is the vacuum permittivity, $n(\omega)$ and $n(\Omega)$ are the indices of refraction at optical and THz frequencies, $\Delta n \equiv n(\Omega) - n_g$ is the difference between the THz index and the optical group index, L is the length of the crystal, $\alpha(\Omega)$ is the frequency-dependent absorption coefficient, $\Delta k = 2\pi/\Lambda_{QPM} \times (\Omega - \Omega_{PM})/\Omega_{PM}$ is the phase mismatch, Λ_{QPM} is the poling period and $\Omega_{PM} = 2\pi c/\Delta n \Lambda_{QPM}$ is the phase-matched THz angular frequency. The saturation behavior with length is captured by the term in brackets which we can define an effective interaction length in the absence of pump:

$$L_{eff}(\alpha, L) \equiv \left[\frac{1-e^{-\alpha(\Omega_{PM})L}}{\alpha(\Omega_{PM})}\right]. \tag{2}$$

This expression shows that the effective length approaches the absorption length for $L \gg 1/\alpha$ and also shows that the saturation efficiency is inversely proportional to the absorption coefficient:

$$\eta_{sat} \equiv \frac{4d_{eff}^2\Omega_{PM}^2 F_0 L_{abs}}{\pi^2\varepsilon_0 c^2 n^2(\omega) n(\Omega_{PM}) \Delta n} e^{-\frac{1}{2}(\Omega_{PM}\Delta T)^2}. \tag{3}$$

This saturation behavior, however, neglects the strong modification of the optical pump during propagation, due to the high optical intensities and the strongly nonlinear response of the crystal. Although the pump depletion resulting from THz generation is minor, the pump spectrum and phase can be strongly modified. Other parasitic nonlinear processes like self-phase modulation (SPM), second harmonic generation (SHG), and "green-induced infrared absorption" (GIIRA) resulting from SHG can also be expected to have a strong effect, and, indeed strong absorption of the pump was observed in the measurements. The efficiency should therefore decrease for crystal lengths significantly beyond L_{abs}. Since the degree of pump modification scales with intensity and propagation distance, it is clear that the saturation fluence and peak efficiency should decrease with crystal length. Such dependences have also been reported previously [13].

Based on measurements in the literature [30,35], the absorption coefficient is α_{LiNbO_3}(300K, 300 GHz) $\approx$ 7.6 cm^{-1} at RT and α_{LiNbO_3}(80K, 340 GHz) $\approx$ 0.76 cm^{-1}, at CT, where the difference in phase-matched THz frequency with temperature has been accounted for. The associated absorption length scales are then L_{LiNbO_3}(300K, 300 GHz) $\approx$ 1.3 mm and L_{LiNbO_3}(80K, 340 GHz) $\approx$ 13 mm, respectively. For room temperature, all crystals tested were much longer than the absorption length, while at cryogenic temperature, the shortest crystal was equivalent to the absorption length. This simple analysis agrees qualitatively with the experimental result of the best performance for the shortest crystal.

To test this behavior more quantitatively, one-dimensional (i.e., excluding transverse dynamics) numerical simulations of the THz generation were conducted which included the effects of pump depletion and self-phase modulation [7] (Figs. 2(c) and 2(f) for RT and CT, respectively). These simulations show a similar trend in that yield, peak efficiency and saturation fluence decrease with length and are improved by going to cryogenic temperature. What is also evident in the simulations are the effects of the difference in THz absorption length between RT and CT. At

Optics EXPRESS

RT, the absorption length is so short that there is no benefit to increasing the device length, even for low fluences where pump modification is minimized. Expressing this quantitatively, for the range of device lengths tested we have $9<L/L_{abs}<30$, so that $0.9999<\eta(L)/\eta_{sat}<1$. The effect of length on efficiency is therefore negligible in this regime. The simulations confirm a similar CE for all device lengths at low fluence but a decreasing performance with length due to pump depletion higher fluences. These features are coarsely reproduced in the data. By contrast at CT, the saturation length is much longer so that in the absence of pump modification, there is still an advantage to increasing the interaction length. Quantitatively, we have $0.9<L/L_{abs}<3$, so that $0.60<\eta(L)/\eta_{sat}<0.94$. Once again, the simulations confirm the expectations that at low fluence, the CE increases with length, while at high fluence, it decreases with length due to pump depletion. This cross-over behavior is evident in the data although there are disagreements in the cross-over fluence and the magnitude of the CE.

In general, there are large disagreements in the magnitude of the yield and conversion efficiencies of a factor of up to 4x for the RT case and over 10x for the CT case. The saturation fluence in the simulations is also roughly a factor of 5x – 10x higher than in experiments. These disagreements imply that the interaction with the PPLN crystals causes a much higher degree of modification of the pump pulse than predicted by the numerical model. For the RT case, there is also a large jump in performance between the 12 mm and 16 mm devices which is not reproduced in the simulation.

To evaluate these discrepancies more quantitatively, the simulations were plotted together with the data for each device, using a scaling factor to achieve agreement at low fluence (Fig. 3). For all cases, the scaling factor was chosen to match the CE at the lowest measured fluence. The results show several important trends. First, the large jump in performance between the 12 mm and 16 mm devices at RT is not reflected in the scaling factor which is very similar for all lengths. The discrepancy between experiment and simulation at higher fluences, however, does show a substantial difference between the 12 mm and 16 mm devices, pointing to pump modification as a culprit. In general, the discrepancy increases dramatically with fluence for all crystals and both temperatures. This growing discrepancy agrees with the interpretation of increasing pump modification with fluence and interaction length. However, the necessity of using scaling factors significantly less than 1.0 indicates a disagreement even at the lowest fluences where the undepleted pump approximation might be expected to hold. This suggests that the threshold fluence for significant pump modification may be quite low in this configuration. As expected, the disagreement occurs sooner (i.e., at lower fluence) for longer crystals, especially at RT where, due to THz absorption, it is the modified pump at the end of the crystal that is primarily responsible for the yield. Finally, it is apparent that the slope efficiency (i.e., the dependence of efficiency on fluence), as determined at the lowest fluences, is 3 – 6x farther from prediction at CT than at RT.

Given that this model has successfully predicted efficiencies in previous experiments using long, temporally-modulated laser pulses [6,8,9], the large discrepancies points to the presence of additional (most likely nonlinear) effects not included in the model which arise for the high intensities associated with the use of a single short, compressed pulse driver. Among these is SHG, since copious amounts of green light typically accompany the THz generation in this regime. Further evidence of unaccounted-for nonlinear effects is the observation of strong, fluence-dependent attenuation of the driver pulse transmitted through the PPLN crystal which, in the extreme case, reached up to 90%. Considering the sub-percent level of THz generation, pump-depletion associated with this process cannot account for this level of attenuation of the transmitted pump. Another, process such as GIIRA, must therefore be at play. A thorough investigation of additional processes is therefore merited in order to fully understand and quantitatively predict the THz generation in this regime, but that analysis is beyond the scope of the present work.

Optics EXPRESS

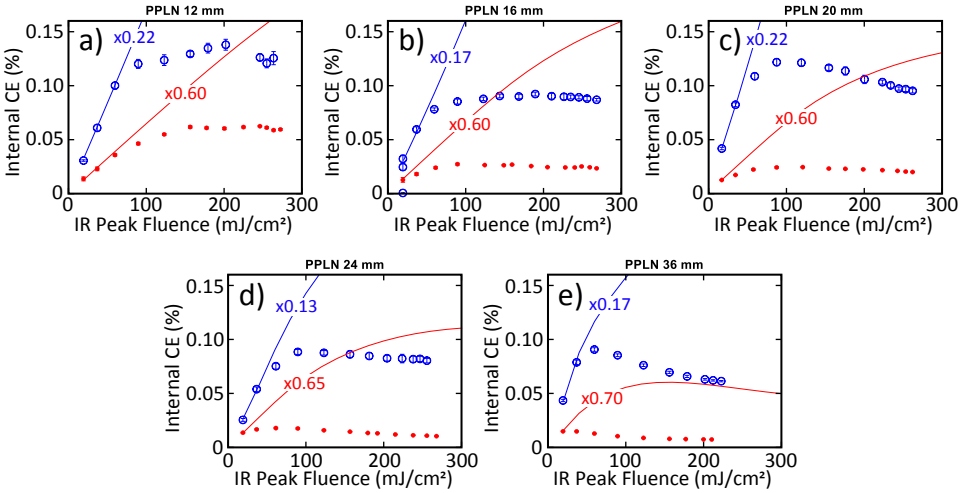

Fig. 3. Comparison of data and simulation for large-aperture PPLN devices. (a)–(e) are analyses of devices with lengths 12 mm, 16 mm, 20 mm, 24 mm and 36 mm, respectively. In each panel, the RT data (simulations) are shown as red dots (lines), while the CT data (simulations) are shown as blue circles (lines). The number intersecting each line is the scaling factor required to have the simulations agree with the data at low fluence.

3.2. *Results using wafer-stack devices*

To complement the measurements using the voltage-poled crystals, a set of experiments were performed using four distinct wafer stacks of three different kinds. The specifications of these stacks are summarized in Table 2.

Table 2. Summary of wafer-stack specifications

Device	Material	Aperture	Wafer thickness	Max no. wafers	Expected Frequencies	
					RT	CT
stack 1	[a]5% MgO:$LiNbO_3$	1" diam.	300 μm	31	172 GHz	n.a.
stack 2	[b]5% MgO:$LiNbO_3$	25×26 mm^2	200 μm	42	258 GHz	279 GHz
stack 3	[c]KTP	10×10 mm^2	250 μm	22	286 GHz	314 GHz
stack 4	[b]KTP	10×10 mm^2	250 μm	38	286 GHz	314 GHz

[a]Manufacturer #1
[b]Manufacturer #2
[c]Manufacturer #3

Stack 1 was composed of round wafers of 5% MgO-doped $LiNbO_3$ of thickness 300 μm and diameter 25.4 mm; stack 2 was composed of rectangular wafers of 5% MgO-doped $LiNbO_3$ of thickness 200 μm and aperture 25 mm x 26 mm; and stacks 3 and 4 were composed of square wafers of KTP from two different vendors, of thickness 250 μm and aperture 10 mm x 10 mm. A summary of the yield for these three stack types is shown in Fig. 4. Stack 1 was only characterized at RT due to its round cross-section which made achieving good thermal contact with the cold surface of the cryostat impractical. Stacks 2 and 4, however, were characterized at both RT and CT. Stack 3 was only used for the length-dependence characterization at RT, as in subsequent measurements the AR coatings were damaged, rendering them unsuitable for further experiments.

As with the voltage-poled devices, the yield was measured as a function of incident fluence (1st and 2nd columns) and crystal length (3rd column). The fluence scans were performed for

Optics EXPRESS

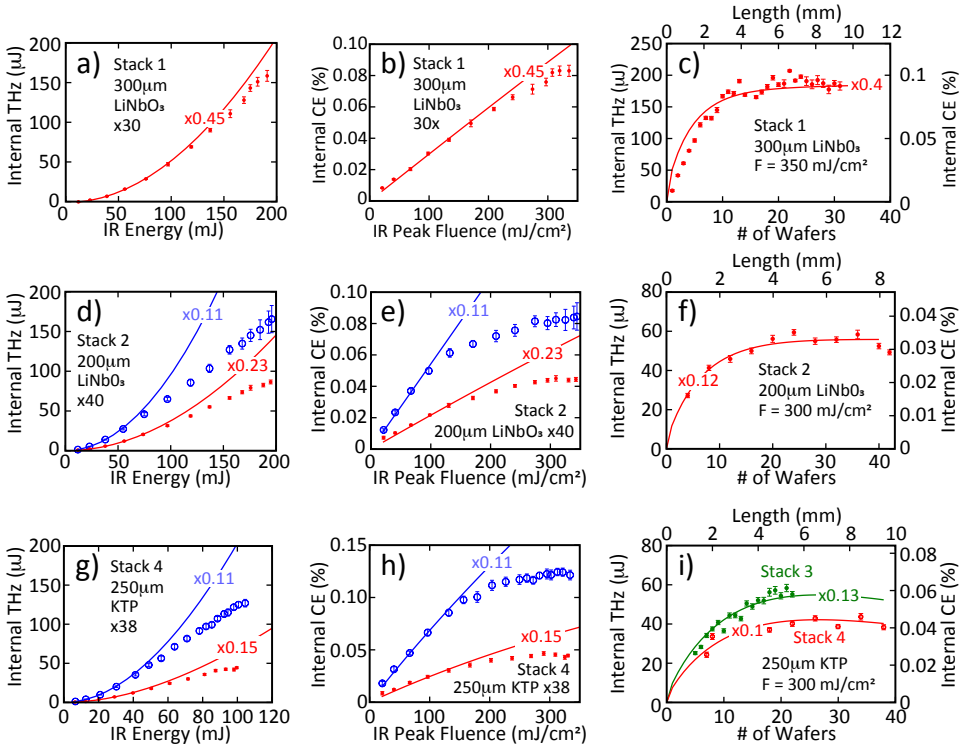

Fig. 4. THz yield for the four wafer stacks (see Table 2 for specifications). The top row corresponds to wafer stack 1 (300μm $LiNbO_3$), the middle row to wafer stack 2 (200μm $LiNbO_3$), and the bottom row to stacks 3 and 4 (250μm KTP). The left column presents the internal THz yield vs the incident IR pulse energy; the middle column is the internal CE vs the IR peak fluence, calculated from the data in the left column; and the right column is the THz yield and CE vs number of wafers and crystal length. The energy scans in (a), (d) and (g) were performed for stacks of 30, 40 and 38 wafers, respectively, while the wafer-number scans in (c), (f) and (i) were performed at peak fluences of 350 mJ/cm^2, 300 mJ/cm^2 and 300 mJ/cm^2, respectively. The energy-scan results in panels (g) and (h) correspond to wafer stack 4, while the wafer-number-scan results in (i) correspond to stack 3 (in green) and stack 4 (In red). RT measurements are plotted in red, while CT measurements are in blue. The data is plotted as markers with vertical error bars, while corresponding simulations are plotted as lines of the same color. The simulation results were all scaled by a factor, shown in each panel, in order to aid comparison with the data.

stacks of 30 wafers, 40 wafers and 38 wafers for stacks 1, 2 and 4, respectively, corresponding to similar interaction lengths of 9 mm, 8 mm and 9.5 mm, respectively. We first compare the stacks from the perspective of maximum THz yield (Figs. 4(a),(d),(g)) to evaluate our success in scaling to large apertures. At RT, Stack 1 produced the highest internal yield of over 160 μJ, compared to 86 μJ and 45 μJ for stacks 2 and 4, respectively. Going to CT improved the performance of stacks 2 and 4 to 170 μJ and 130 μJ, respectively. It should be noted that while the 25.4 mm diameter of stack 1 and the 25×26 mm aperture of stack 2 were large enough to accept the full energy of the pump beam, the 10×10 mm aperture of stack 4 (chosen based on cost considerations) limited the incident pump pulse energy to only 53% of the total. Thus, by increasing the size of the KTP wafers to the 1-inch level (which is possible using existing commercial sources) at least 30% increase of the yield to ~260 μJ would likely have been achieved. To evaluate the performance independently of the aperture size, we also plotted the CEs for each wafer stack (Figs. 4(b),(e),(h)).

Optics EXPRESS

The maximum CEs achieved at RT were 0.085%, 0.045% and 0.047% for stacks 1, 2 and 4, respectively. At CT the CE of stacks 2 and 4 improved by ~1.9x and ~2.7x, respectively, to 0.084% and 0.125% respectively. This improvement in performance with temperature is clear evidence that the cryogenic cooling was effective despite the small cross-sectional area of an individual wafer.

The flexibility of the stacking process also enables a detailed exploration of the length dependence of the yield with fine resolution. In Figs. 4(c),(f),(i), the dependence of the yield and CE on number of wafers was studied at a peak fluence of 350 mJ/cm^2 for stack 1 and at 300 mJ/cm^2 for the other stacks. This measurement was only done at RT due to the impracticality associated with changing the wafer number inside a cooled cryostat. The results show that the CE initially increases with interaction length, but saturates at a relatively short value of 3–4 mm corresponding to less than 20 wafers. Considering the short absorption lengths at RT (1.3 mm for $LiNbO_3$, and 2.8 mm for KTP), a short saturation length is to be expected. Comparison with simulation shows that despite a large discrepancy in overall yield, the behavior with length is very similar, roughly confirming the absorption length. This agreement is least close for wafer stack 1 which appears to have a longer absorption length than predicted, implying a lower absorption coefficient. For all stacks, the maximum efficiency is reached slightly after the saturation length and before the maximum length of the crystal, which is consistent with the model that the yield for longer lengths is reduced by pump modification. It should be noted that the fluence scan data were taken for the longest wafer stacks, so that the peak performance for the fluence scans and the wafer-number scans were not the same. In the case of stack 1, the best performance was obtained for an intermediate number of 22 wafers with a yield of over 207 μJ and a CE of 0.10%. These figures exceed those of the fluence scan data taken with 30 wafers. The wafer-number studies of the other stacks show a similar maximum for wafer numbers of about 20 and lengths of about 5 mm.

Simulations were performed for all cases to compare with the data (depicted by the solid lines in each panel of Fig. 4). In order to enable comparisons with the PPLN devices in the previous section, the simulations treated the wafer stacks as ideal in that the losses between wafers were neglected as well as any deviations from perfect periodicity in the poling. As for the voltage-poled devices, the simulations show large discrepancies with the data in both the predicted yield and in the saturation behavior. For the energy and fluence scans (Figs. 4(a),(b),(d),(e),(g),(h)), the predicted yield is over-estimated by a factor of 2 – 10x, as can be seen by the value of the scaling factor (shown in each graph) used to make the simulations agree with the experiments at low fluence. The agreement generally appears to be better at higher temperature and lower frequencies. For the wafer-number scans (Figs. 4(c),(f),(i)), the shape of the dependence of yield on length matches quite well between data and simulation despite the discrepancy in scale. For the three cases, the dynamics with interaction distance seem to be dominated by the saturating effect of absorption, as described in the heuristic model in the previous section.

3.3. Comparison of all devices

A summary of the performance of all devices tested is shown in Table 3 for the fluence-scan data. Devices tested at RT are shown in red while those tested at CT are in blue. Direct comparison of the device performance is complicated by disparities in multiple parameters, including the aperture, available pump energy, the device length, and the phase-matched frequency. A full evaluation therefore requires comparison on the basis of multiple metrics. In terms of absolute yield, stack 2 ($LiNbO_3$, 400 μm poling) at RT produced the highest THz pulse energy of 170 μJ, followed by stack 1 ($LiNbO_3$, 600 μm poling) which produced 160 μJ at RT. These two stacks had the largest apertures of all devices tested. Stack 3 (KTP, 400 μm poling) came in 3rd yielding only 127 μJ at CT due to the aperture limitation. Extrapolating to the full energy of the incident pump, however, shows that a larger-aperture KTP wafer stack could have produced ~240 μJ at

Optics EXPRESS

CT, exceeding the output of the other stacks. Comparing the devices in terms of efficiency shows that, indeed, among the wafer stacks, stack 4 at CT performed the best, with 0.13% internal CE at a fluence of 320 mJ/cm^2. The 12 mm-long large-aperture PPLN device at CT (which performed the best out of the PPLN devices), demonstrated the overall highest internal CE of 0.14% at a fluence of 200 mJ/cm^2.

Table 3. Summary of device fluence-scan performance

Device	Material	Poling Period [μm]	Expected Frequency [GHz]	Max pump energy [mJ]	Max Yield [μJ]	Max Efficiency [%]	Max Slope Efficiency [%/(mJ/cm^2)]	Performance relative to simulation
9 mm Stack 1	$LiNbO_3$ (RT)	600	172.1	195	160	0.085	3.0×10^{-4}	0.45
8 mm Stack 2	$LiNbO_3$ (RT)	400	257.5	195	86	0.045	2.2×10^{-4}	0.23
8 mm Stack 2	$LiNbO_3$ (CT)	400	279.0	195	170	0.085	5.4×10^{-4}	0.11
8.5 mm Stack 4	KTP (RT)	500	286.3	105	45	0.047	2.5×10^{-4}	0.15
8.5 mm Stack 4	KTP (CT)	500	314.1	105	127	0.125	7.1×10^{-4}	0.11
12 mm PPLN	$LiNbO_3$ (RT)	330	312.2	85	51	0.063	6.3×10^{-4}	0.60
12 mm PPLN	$LiNbO_3$ (CT)	330	337.8	85	104	0.140	17.0×10^{-4}	0.22

These performance figures include the effect of differences in phase-matched frequency and in crystal length. In addition, there is a very strong impact from the saturation of the efficiency with fluence, which, as discussed above is connected to nonlinear modification of the optical pump. The plots in Fig. 4 show that the effect of saturation is stronger for CT than for RT, and was weakest for stack 1, which also supported the lowest frequency. Comparing the middle columns of Fig. 2 and Fig. 4, we can see that the CE in the wafer stacks saturates at a higher fluence (200–300 mJ/cm^2) than for the voltage-poled devices (50–150 mJ/cm^2), which may be connected to the shorter interaction lengths.

An alternate assessment of the device performance that neglects the effects of saturation can be done by examining the slope efficiency. Using this metric, we see that, once again, stack 4 (KTP) at CT performed best of the wafer stacks, with a slope efficiency of 7.1×10^{-4} %/(mJ/cm^2). However, if we account for the differences in phase-matched frequency (which, based on Eq. (1), we can estimate by scaling by the frequency squared), we find that the performance of stacks 2 and 4 were actually comparable. The 12 mm PPLN at CT, on the other hand, had a significantly higher slope efficiency of 17.0×10^{-4} %/(mJ/cm^2). The 12 mm PPLN at RT also performed better than all the wafer-stacks at RT.

As a final metric, we calculate the ratio of the measured and simulated slope efficiencies to estimate how well the devices performed relative to expectation in a regime where saturation effects are minimized. This metric accounts for all parameter disparities including the length which, as shown by Fig. 2(f), strongly affects the slope efficiency at CT due to the long saturation length. As shown by the values in the right-most column of Table 3, all devices performed closer to expectation at RT vs CT. Of the wafer stacks, stack 1 performed significantly better than the others. The fact that this device also suffered the least from saturation effects hints that pump modification may be affecting performance even at low fluence. The 12 mm PPLN device outperformed all wafer stacks both at RT and at CT, indicating that the manual poling process is likely responsible for some performance loss. Finally, comparing wafer stacks 2 and 4 we see that the $LiNbO_3$ stack was closer to expectation than the KTP stack at RT but equivalently close at CT. Combined with the analyses in terms of efficiency and slope efficiency, this result indicates that KTP is a viable alternative to $LiNbO_3$ and can even outperform it.

Optics EXPRESS

3.4. Comparison of KTP and $LiNbO_3$

The relative performance of KTP and $LiNbO_3$ can be predicted using Eq. (1). Assuming two crystals of the same aperture, length and phase-matched frequency, we can simplify the expression for the slope efficiency to the following:

$$\frac{\partial \eta}{\partial F} \propto \frac{d_{eff}^2}{n^2(\omega) n(\Omega_{PM}) \Delta n} L_{eff}(\alpha, L). \tag{4}$$

For very large values of α, we can approximate $L_{eff} \approx 1/\alpha = L_{abs}$, and we see that the interaction length is limited by the absorption length. By contrast, for very small values of α, we can approximate $L_{eff} \approx L$, which indicates that the interaction length is set by the crystal length. The performance of KTP relative to $LiNbO_3$ can then be calculated using Eq. (2) by taking the ratio of the two slope efficiencies:

$$\mathcal{R} \equiv \frac{\partial \eta / \partial F_{KTP}}{\partial \eta / \partial F_{LiNbO_3}} \tag{5}$$

Figure 5 shows the value of $\mathcal{R}$ for the representative frequency of 300 GHz as a function of crystal length at both RT and CT, using the crystal parameters summarized in Table 4. The graphs show that for crystal lengths beyond a couple of millimeters we should expect KTP to perform better than $LiNbO_3$ at both RT and CT. The lower value of d_{eff} for KTP relative to $LiNbO_3$ is more than compensated by lower values of the indices of refraction as well as the absorption coefficient, resulting in an overall better efficiency. At RT, the efficiency ratio saturates for lengths above 15 mm at a maximum value of $\mathcal{R}_{max}^{RT} \approx 1.43$, whereas at CT, the ratio continues to increase with length beyond 50 mm. These calculations should be interpreted with caution as they are strongly affected by the values of the absorption coefficient for the two materials which, to this day, are not very precisely known at these frequencies and temperatures. This caveat notwithstanding, we use a similar calculation to compare the performance of stacks 2 and 4 (but account for the differences in frequency and crystal length using Eq. (1)) we find measured (calculated) performance ratios of $\mathcal{R}_{meas}^{RT} = 1.14$ ($\mathcal{R}_{calc}^{RT} = 1.65$) at RT and $\mathcal{R}_{meas}^{CT} = 1.31$ ($\mathcal{R}_{calc}^{CT} = 1.56$) at CT. The measurements therefore support the prediction of improved performance in KTP, albeit to a lower extent than predicted. Of course, it must be remembered that the calculations do not account for pump modification which is a strong effect or for differences in the propensity of each material to cause pump modification.

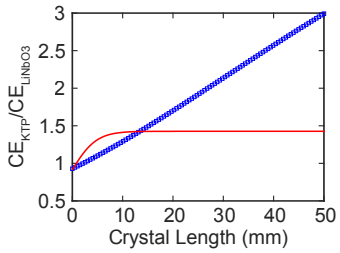

Fig. 5. Ratio of expected slope efficiency for KTP and $LiNbO_3$ at RT (red line) and at CT (blue squares).

3.5. Analysis of THz frequency spectra

A key metric for testing the performance of a periodically-poled crystal is the emission spectrum. Ideally, the center frequency should match the predictions of quasi-phase-matching theory, verifying the poling period, while the bandwidth should provide a diagnostic of the number of

Optics EXPRESS

Table 4. Material parameters for KTP and $LiNbO_3$

Material	d_{33}[pm/V]	$n(\omega)$	$n_g(\omega)$	$n(\Omega_{PM})$	Δn	$\alpha(\Omega_{PM})$ [1/cm]
$LiNbO_3$ (RT)	168 [18]	2.15	2.21	5.12	2.91	7.05
KTP (RT)	105 [36]	1.83	1.88	3.97	2.10	4.49
$LiNbO_3$ (CT)	168 [18]	2.15	2.21	4.89	2.69	0.83
KTP (CT)	105 [36]	1.83	1.87	3.78	1.91	0.11

periods and of the poling regularity. Given the susceptibility of the manual poling process to errors, it is especially relevant to test how closely the spectrum of the THz emitted from the wafer stacks matches expectations. Here the THz spectrum was obtained by interferometric autocorrelation using a Michelson interferometer, measuring the output signal vs delay of one arm, and taking the Fourier transform of the resultant interferogram. Figure 6 shows the interferograms and corresponding (calculated) emission spectra for both the voltage-poled and wafer-stack devices.

The interferograms in Fig. 6(a) show a high degree of structure and persistence over a range of delays greater than should be expected based on the heuristic picture described above and confirmed experimentally by Mosely et al. [26] of one THz cycle being created per poling period of the crystal. In particular, the temporal structure shows evidence of multiple pulses offset by various delays in the range of 10s to 100s of picoseconds, corresponding to longitudinal separations in the range of a few millimeters to a few centimeters. The associated peaks in the power spectra (Fig. 6(c)) correspondingly show modulation patterns consistent with the presence of multiple pulses. The multiplicity of pulses is attributable to Fresnel reflections within the beam splitter which was a 3.5 mm thick, plane-parallel slab of silicon. To understand the effect of the beam splitter on the measurement, an analytic and numerical model was made of the interferometric measurements. First, analytical derivations were made of the expected spectral field of the THz pulses emitted by the crystals as well as of the full (complex) reflection and transmission functions of the beam splitter. The spectral field expression, using the same analytical approach as for Eq. (1) [8,12,17], is given below:

$$A_{THz}(\Omega, L) \approx \frac{\sqrt{8} d_{eff} \Omega I_0 \Delta T}{\varepsilon_0 \pi^2 c^2 n(\omega) n(\Omega)} e^{-\left(\frac{1}{2}\Omega \Delta T\right)^2} \frac{e^{i\Delta k(\Omega)L} - e^{-\frac{1}{2}\alpha(\Omega)L}}{\frac{1}{2}\alpha(\Omega) + i\Delta k(\Omega)} \tag{6}$$

The complex reflection and transmission coefficients for the beamsplitter, which can be derived straightforwardly, are given below:

$$R_{tot} = r_{01}\left(\frac{e^{i\phi_{RT}} - 1}{1 - r_{01}^2 e^{i\phi_{RT}}}\right) \tag{7}$$

$$T_{tot} = e^{i\phi_1}\left(\frac{1 - r_{01}^2}{1 - r_{01}^2 e^{i\phi_{RT}}}\right) \tag{8}$$

where $r_{01} = (\cos\theta_{inc} - n\cos\theta_{refr})/(\cos\theta_{inc} + n\cos\theta_{refr})$ is the Fresnel reflection coefficient for an s-polarized wave incident on the beam-splitter of index $n = 3.425$, and $\theta_{inc} = 45°$ and θ_{refr} are the angles of incidence and refraction. The phase terms are given by $\phi_{RT} = 2kd\cos\theta_1$ and $\phi_1 = kd\sec\theta_1$, where $k = \Omega/c$ is the THz wave vector and d is the beam-splitter thickness.

These analytical expressions were then numerically implemented to generate predictions for the interferograms and the resultant Fourier-transform-based power spectra (Fig. 6(b) and Fig. 6(d), respectively). Visually, both the interferograms (which were cropped to match the range of the measurements) as well as the resultant spectra show a decent match between the measurements

Optics EXPRESS

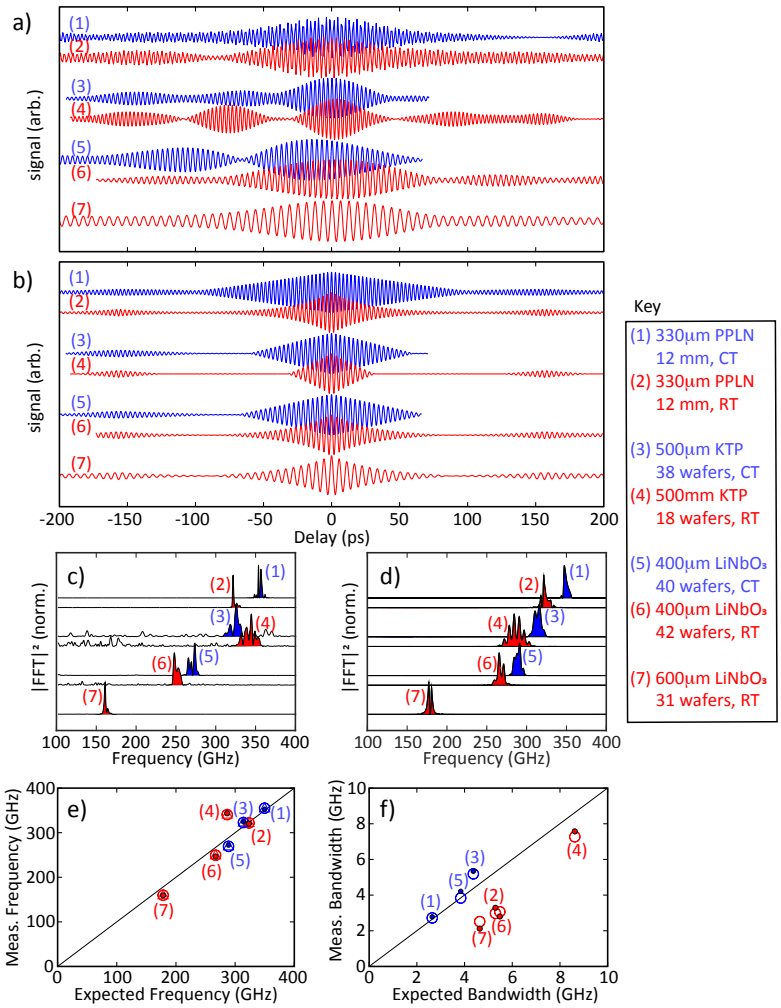

Fig. 6. Spectral characterization of the THz radiation emitted from both the LA-MgO: PPLN and wafer stack devices. (a) Interferometric autocorrelations measured for all devices. Red and blue traces correspond to RT and CT conditions, respectively. For ease of interpretation, the traces presented here were spectrally filtered to include only contributions from a window around the main peak in the Fourier transform associated with the THz emission. (b) Calculated interferometric autocorrelations for the devices in (a) using an analytic and numerical model including the effects of phase-matching and the reflections in the beam-splitter of the interferometer. (c) Power spectra of the THz pulses calculated from the modulus squared of the Fourier transform of the interferograms in (a). Traces filled with red (blue) correspond to RT (CT) conditions. The filled regions of each trace correspond to the acceptance window for the spectral filtering process described in (a). (c) Comparison of the measured and expected center frequencies for all devices. (d) Power spectra for the calculated interferograms in (b). (e) The locations of the peaks in the graphs of (c) and (d) plotted against the expected phase-matching frequency. The black line represents the expected values; red (blue) dots represent the RT (CT) peak values from (c); red (blue) triangles represent the RT (CT) centroid values from (c); red (blue) circles represent the RT (CT) peak values calculated from cropped versions of the interferograms in (a) where only the central part of the interferogram, corresponding to the primary pulse, was kept (the acceptance window was judged visually by finding the location of the minimum fringe intensity within a range of +/-100 ps from zero. (f) same as (e), but plotting the measured vs expected peak widths (standard deviation) from the traces in (c) and (d).

Optics EXPRESS

and the model, both in the presence of multiple pulses in the interferograms as well as in the modulation of the spectra. To evaluate the results more quantitatively, the positions and widths of the peaks in Figs. 6(c),(d) were plotted with measured values on the y-axis and expected values on the x-axis (Fig. 6(e) and Fig. 6(f), respectively). In Fig. 6(e), the black reference line represents the phase-matched frequencies obtained from the analytic expression, while the peak and centroid values from the data are plotted as red dots and triangles for RT and as blue dots and triangles for CT. The measured center frequencies correspond reasonably well to the expected values, showing that the desired poling structure was successfully achieved. In addition, since both CT and RT data are included in the plot, it can be seen that the shift in frequency between RT and CT occurs as expected, proving that the cooling of the wafer stacks was effective. Figure 6(f), which uses the same color and marker scheme as Fig. 6(e), shows that the bandwidths of the measured spectra correspond well to expectation for the CT data, but less well for the RT data. The reason for this inconsistency is not clear, however the systematic difference between the CT and RT data could be explained by an error in the coefficients of absorption for the materials, which would affect the RT results more than the CT results. The discrepancy is also unlikely to be attributed to the wafer-stacking procedure, as the voltage-poled device showed a similar effect.

The effect of the reflections from the beam-splitter on the measurement were also evaluated to make sure that they did not overly influence the conclusions. In Figs. 6(e),(f), the peak values and standard-deviation bandwidths, respectively, from the model spectra in Fig. 6(d) are plotted as black dots. Despite the modulations to the spectra, these line up very well with the predicted values. As a further analysis, the measured interferograms from Fig. 6(a) were cropped to include only the central portion corresponding to the primary pulse, and the peak positions and widths were recalculated (red and blue circles in Figs. 6(e),(f)). The cropping was done visually by identifying the points of minimum fringe amplitude within the range of +/- 100 ps. The results of this analysis are very similar to the analysis of the full interferograms, showing that the beam-splitter reflections did not strongly influence the results.

4. Discussion and conclusions

We explored scaling of DFG-based multicycle THz generation to high pulse energies in a set of novel, large-aperture, periodically-poled crystals of varying period, length, aperture and material. These crystals included both custom, large-aperture (10 mm) voltage-poled $LiNbO_3$ as well as 10–25 mm-aperture manually-stacked macro crystals of $LiNbO_3$ and KTP. The experiments using the (330 μm period) voltage-poled devices represent the first "optical rectification"-type measurements of THz generation (i.e., driving with single, compressed pulses) at such large-apertures. We also extend on previous efforts with the wafer-stack approach by increasing the stack length by a factor of three, by implementing cryogenic cooling and by testing an alternate material, namely KTP. In addition, we present a detailed quantitative analysis of the efficiency trends by comparing measurements with simulation and comparing the performance of the devices to each other.

Our results confirm a successful scaling of the multicycle THz generation process to large apertures. Unsurprisingly, the largest aperture devices produced the highest yield as they accepted the largest fraction of the incident energy. For the voltage-poled PPLN devices, the highest yield of over 100 μJ was achieved for the shortest length (12 mm) at CT yielding 355 GHz pulses with internal energies of over 100 μJ corresponding to a CE of over 0.14%. Using wafer stacks, the highest yield of over 200 μJ was obtained from a stack of twenty-two 25.4 mm diameter, 300 μm thick $LiNbO_3$ wafers at RT (160 GHz), with a corresponding CE of 0.1%. The CEs achieved for these large-aperture devices were in a similar range as those previously achieved with smaller, commercially available devices [13]. In addition, the spectral analysis showed that the central frequency and bandwidth are mostly in line with expectation. Together, the CE and spectrum analyses confirm that both the voltage-poled devices and the wafer-stack devices are viable as

Optics EXPRESS

large-aperture quasi-phase-matching media for narrowband THz pulse generation via nonlinear down-conversion and produced pulse energies significantly beyond what has been achieved with smaller commercial devices.

Comparison of the performance of the devices with simulation shows that the numerical model significantly overestimates the THz yield by factors up to 10x even at low fluence where the undepleted pump approximation is relevant. This discrepancy, which tends to be greater at CT than at RT, increases significantly for higher fluence and greater interaction lengths resulting in saturation and eventually reduction of the CE. It should be noted that for previous experiments performed using longer (temporally-structured) pulses, very good agreement has been demonstrated between experiment and simulation [6] using the same code. A key difference from those experiments is the peak intensity which, when driving with a single, short pulse, is tens-to-hundreds of times higher. These factors point to severe pump modification via nonlinear processes other than THz generation as a likely culprit for the discrepancy. Unfortunately, very little literature exists which quantitatively compares measured THz yield with expectations from simulation. These comparisons are essential for developing a quantitative model to describe pump modification and the saturation process which limits the peak fluence (especially for the 1-pulse driver configuration) and is the ultimate driver of the need to scale apertures. Such a model is currently lacking. In previous work, we recently explored the parameter-dependence of the discrepancy using flexibly-configurable pulse trains as drivers [8], and here, we extend upon that analysis by exploring the parameter dependence of the discrepancy for single-pulse drivers. However, much more work is needed to isolate the specific nonlinear processes (e.g., SHG, SPM, PRE, GIIRA and Raman scattering among others) and quantify their relative contributions to the saturation process.

Analysis of the relative performance of the devices was also highly fruitful. We found that at RT, the lowest-frequency wafer stack (stack 1) provided the highest CE of all devices, while at CT, the 12 mm voltage-poled PPLN had the best CE. Meanwhile, among the wafer stacks, the KTP stack performed best at CT highlighting the benefit of exploring alternative materials. However, given the disparity in the parameters of each device (e.g., number of wafers, aperture size and phase-matched frequency), direct comparisons on the basis of yield or CE are somewhat misleading. We therefore developed a metric based on comparisons with simulation for the slope efficiency at low fluence. This analysis showed that the 12 mm voltage-poled device performed best (i.e., closest to prediction) both at RT and at CT and confirmed that, in general, the devices performed closer to prediction at RT than at CT. The distinction between RT and CT performance was observed in multiple domains. Beyond the CE being closer to simulation at RT, we also found that the measured spectral bandwidths were narrower than expected at RT and (for stack 1), the absorption length was also a bit longer than predicted. One possible explanation for all three effects is if the absorption coefficient at RT is lower than expected. In general, the absorption coefficient is a critical parameter governing the dynamics of the THz generation so more precise measurements under working conditions would be of high value, especially for KTP where much less information exists than for $LiNbO_3$.

The results presented here clearly show that scaling to large apertures is feasible with current technologies. However multiple areas of improvement exist for both the voltage-poled and wafer-stack approaches. The wafers currently present an enormous advantage relative to the voltage poled devices in terms of aperture. Further scaling of individual voltage-poled devices to the multiple-centimeter range of apertures seems unlikely to happen anytime soon due to material limitations. The higher performance of the voltage-poled devices relative to simulation, on the other hand, suggests a higher quality of the poling structure compared to the wafer stacks. A potential solution for the wafer-stack approach could be optical bonding which would eliminate the need of AR coatings and reduce the likelihood of inter-wafer gaps caused by dust or wafer curvature. On the other hand, further increases in the effective aperture of voltage-poled PPLN

Optics EXPRESS

devices could be achieved by stacking multiple devices. Exploration of both approaches is merited. Further exploration of periodically-poled KTP is also clearly indicated since the wafer stacks of this material showed slightly better performance relative to the $LiNbO_3$ wafer stacks.

Finally, it should be emphasized that substantial improvements in CE can be obtained for all devices by optimizing the spectral, temporal and spatial properties of the drive laser pulses as has been both numerically [7,12] and experimentally [6,8,9,15] demonstrated. In particular, the use of regular pulse trains is called for with the number of pulses matched to the number of poling periods and the pulse-train burst frequency tuned to the phase-matched THz frequency [8]. In this work, single-pulse drivers were used in order to facilitate testing of multiple devices with disparate quasi-phase-matched frequencies. This benefit, however, came at the expense of strong saturation due to the high intensities and the resultant pump modification which limited the useful fluence. In a pulse-train-pumping configuration, the incident fluence remains the same, but the peak intensity of the driver is dramatically reduced, mitigating much of the pump modification and enhancing the CE. Assuming an improvement of the CE to the 1% level, as has been demonstrated recently [6], THz yields in the range of 1 mJ would then be reached using the laser system in this study. However, for this performance to be realized, substantially longer devices are needed. Such devices have numbers of periods in the range of 100 or more, which is generally not a problem for the voltage-poled devices but is an order of magnitude beyond what has been demonstrated so far for wafer stacks. The work here takes a significant step in the development of such devices by demonstrating stacks of over 40 wafers (20 periods), but another factor of 5x or greater is still needed. Here, KTP presents another advantage. Since its THz index is lower compared to $LiNbO_3$, thicker wafers which are easier to handle can be used to achieve the same frequency, extending the interaction length. As the length of these stacks becomes greater, the necessity of cryogenic cooling will also increase. The results presented here, however, show that cryogenic cooling of wafer stacks is feasible. Further testing of large-aperture devices driven by high-energy pulse trains, both in the voltage-poled and wafer-stack variations, is therefore planned.

Funding. HORIZON EUROPE European Research Council (609920, ERC Synergy Grant "AXSIS", FP7/2007-2013); Deutsche Forschungsgemeinschaft (405983224).

Acknowledgments. Portions of this work were presented at the 10th Tiny Integrated Laser and Laser Ignition Conference 2024 (TILA-LIC 2024), 24-26 April 2024, plenary talk TILA-LIC5-01, paper title "Terahertz Acceleration for Compact Electron and X-Ray Sources".

Disclosures. The authors declare no conflicts of interest.

Data availability. Data underlying the results presented in this paper are not publicly available at this time but may be obtained from the authors upon reasonable request.

References

1. B. Green, S. Kovalev, V. Asgekar, *et al.*, "High-field high-repetition-rate sources for the coherent THz control of matter," Sci. Rep. **6**(1), 22256 (2016).
2. D. Zhang, T. Kroh, F. Ritzkowsky, *et al.*, "THz-Enhanced DC Ultrafast Electron Diffractometer," Ultrafast Sci. **2021**, 9848526 (2021).
3. E. A. Nanni, W. R. Huang, K. H. Hong, *et al.*, "Terahertz-driven linear electron acceleration," Nat. Commun. **6**(1), 8486 (2015).
4. D. Zhang, A. Fallahi, M. Hemmer, *et al.*, "Segmented terahertz electron accelerator and manipulator (STEAM)," Nat. Photonics **12**(6), 336–342 (2018).
5. F. X. Kärtner, F. Ahr, A. L. Calendron, *et al.*, "AXSIS: Exploring the frontiers in attosecond X-ray science, imaging and spectroscopy," Nucl. Instruments Methods Phys. Res. Sect. A Accel. Spectrometers, Detect. Assoc. Equip **829**, 24–29 (2016).
6. H. T. Olgun, W. Tian, G. Cirmi, *et al.*, "Highly efficient generation of narrowband terahertz radiation driven by a two-spectral-line laser in PPLN," Opt. Lett **47**(10), 2374–2377 (2022).
7. K. Ravi, D. N. Schimpf, and F. X. Kärtner, "Pulse sequences for efficient multi-cycle terahertz generation in periodically poled lithium niobate," Opt. Express **24**(22), 25582–25607 (2016).
8. N. H. Matlis, Z. Zhang, U. Demirbas, *et al.*, "Precise parameter control of multicycle terahertz generation in PPLN using flexible pulse trains," Opt. Express **31**(26), 44424–44443 (2023).

Optics EXPRESS

9. W. Tian, G. Cirmi, H. T. Olgun, *et al.*, "μJ-level multi-cycle terahertz generation in a periodically poled Rb:KTP crystal," Opt. Lett. **46**(4), 741 (2021).
10. M. Cronin-Golomb, "Cascaded nonlinear difference-frequency generation of enhanced terahertz wave production," Opt. Lett. **29**(17), 2046–2048 (2004).
11. K. Ravi, M. Hemmer, G. Cirmi, *et al.*, "Cascaded parametric amplification for highly efficient terahertz generation," Opt. Lett. **41**(16), 3806–3809 (2016).
12. K. Ravi and F. X. Kärtner, "Raman Shifting Induced by Cascaded Quadratic Nonlinearities for Terahertz Generation," Laser Photon. Rev **14**(11), 2000109 (2020).
13. S. Carbajo, J. Schulte, X. Wu, *et al.*, "Efficient narrowband terahertz generation in cryogenically cooled periodically poled lithium niobate," Opt. Lett. **40**(24), 5762–5765 (2015).
14. F. Ahr, S. W. Jolly, N. H. Matlis, *et al.*, "Narrowband terahertz generation with chirped-and-delayed laser pulses in periodically poled lithium niobate," Opt. Lett. **42**(11), 2118–2121 (2017).
15. S. W. Jolly, N. H. Matlis, F. Ahr, *et al.*, "Spectral phase control of interfering chirped pulses for high-energy narrowband terahertz generation," Nat. Commun **10**(1), 2591 (2019).
16. F. Lemery, T. Vinatier, F. Mayet, *et al.*, "Highly scalable multicycle THz production with a homemade periodically poled macrocrystal," Commun. Phys **3**(1), 150 (2020).
17. K. L. Vodopyanov, "Optical generation of narrow-band terahertz packets in periodically-inverted electro-optic crystals: conversion efficiency and optimal laser pulse format," Opt. Express **14**(6), 2263–2276 (2006).
18. J. Hebling, K.-L. Yeh, M. C. Hoffmann, *et al.*, "Generation of high-power terahertz pulses by tilted-pulse-front excitation and their application possibilities," J. Opt. Soc. Am. B **25**(7), B6–B19 (2008).
19. J. Hebling, G. Almasi, I. Kozma, *et al.*, "Velocity matching by pulse front tilting for large area THz-pulse generation," Opt. Express **10**(21), 1161–1166 (2002).
20. T. Kroh, T. Rohwer, D. Zhang, *et al.*, "Parameter sensitivities in tilted-pulse-front based terahertz setups and their implications for high-energy terahertz source design and optimization," Opt. Express **30**(14), 24186–24206 (2022).
21. X. Wu, D. Kong, S. Hao, *et al.*, "Generation of 13.9-mJ Terahertz Radiation from Lithium Niobate Materials," Adv. Mater **35**(23), 2208947 (2023).
22. H. Ishizuki, I. Shoji, and T. Taira, "Periodical poling characteristics of congruent MgO:LiNbO3 crystals at elevated temperature," Appl. Phys. Lett **82**(23), 4062–4064 (2003).
23. H. Ishizuki and T. Taira, "Improvement of laser-beam distortion in large-aperture PPMgLN device by using X-axis Czochralski-grown crystal," Opt. Express **22**(16), 19668–19673 (2014).
24. T. Taira and H. Ishizuki, "Large aperture quasi-phase matched nonlinear material for functional power lasers," in *Conference on Lasers and Electro-Optics* (Optica Publishing Group, 2017), paper SW4 M.7.
25. H. Ishizuki and T. Taira, "Half-joule output optical-parametric oscillation by using 10-mm-thick periodically poled Mg-doped congruent LiNbO3," Opt. Express **20**(18), 20002–20010 (2012).
26. C. D. W. Mosley, D. S. Lake, D. M. Graham, *et al.*, "Large-area periodically-poled lithium niobate wafer stacks optimized for high-energy narrowband terahertz generation," Opt. Express **31**(3), 4041–4054 (2023).
27. D. A. Bryan, R. Gerson, and H. E. Tomaschke, "Increased optical damage resistance in lithium niobate," Appl. Phys. Lett **44**(9), 847–849 (1984).
28. M. Hemmer, G. Cirmi, K. Ravi, *et al.*, "Cascaded interactions mediated by terahertz radiation," Opt. Express **26**(10), 12536–12546 (2018).
29. D. E. Thompson, J. D. McMullen, and D. B. Anderson, "Second-harmonic generation in GaAs ''stack of plates'' using high-power CO2 laser radiation," Appl. Phys. Lett **29**(2), 113–115 (1976).
30. L. Pálfalvi, J. Hebling, J. Kuhl, *et al.*, "Temperature dependence of the absorption and refraction of Mg-doped congruent and stoichiometric LiNbO3 in the THz range," J. Appl. Phys **97**(12), 123505 (2005).
31. K. Ravi, F. Ahr, G. Cirmi, *et al.*, "Pulse sequences for high-energy terahertz generation," in *41st International Conference on Infrared, Millimeter, and Terahertz waves* (2016), pp. 1–2.
32. R. J. Bolt and M. van der Mooren, "Single shot bulk damage threshold and conversion efficiency measurements on flux grown KTiOPO4 (KTP)," Opt. Commun. **100**(1-4), 399–410 (1993).
33. W. Wang, Z. Cong, X. Chen, *et al.*, "Terahertz parametric oscillator based on $KTiOPO_4$ crystal," Opt. Lett. **39**(13), 3706–3709 (2014).
34. K. Ravi and F. X. Kärtner, "Terahertz-induced cascaded interactions between spectra offset by large frequencies," Opt. Express **27**(14), 19254–19269 (2019).
35. M. Unferdorben, Z. Szaller, I. Hajdara, *et al.*, "Measurement of Refractive Index and Absorption Coefficient of Congruent and Stoichiometric Lithium Niobate in the Terahertz Range," J. Infrared, Millimeter, Terahertz Waves **36**(12), 1203–1209 (2015).
36. J. D. Bierlein and H. Vanherzeele, "Potassium titanyl phosphate: properties and new applications," J. Opt. Soc. Am. B **6**, 622 (1989).